Bionic Optimization And Aerodynamic Performance Analysis Of High-speed Train Pantograph

Qi Zhou, Zhenfeng Wu*, and Longhui Zhu

School of Mechanical and Electrical Engineering, Lanzhou Jiaotong University, Lanzhou, China

Corresponding author. E-mail: wzhf@mail.lzjtu.cn

Received: August 5, 2023; Accepted: September 22, 2023

The aerodynamic drag of a high-speed train has a significant impact on its energy consumption. At high speeds, the pantograph is one of the primary sources of aerodynamic drag for the train. To enhance train operation characteristics and reduce aerodynamic drag, two optimized pantograph models with bionic non-smooth grooves beneath carbon slide plates were designed based on bionic non-smooth theories, using shark skin as the bionic object. The Navier-Stokes equation and k-ϵ turbulence model were adopted to simulate the flow field structure of two pantograph optimized models. The results show the structure of pantograph head has a significant effect on its separation point of the boundary layer, the wake flow and the tail vortex area. Compared to the pantograph head with arc-shaped grooves, the pantograph head with V-shaped grooves exhibits a more significant backward movement of the boundary layer of separation point. This results in a more stable wake flow and a more pronounced reduction in the area of the tail vortex. Furthermore, incorporating V-shaped grooves beneath the carbon slide plate resulted in an average rate of drag reduction increase of 4.9% for the pantograph head and 4.7% for the pantograph compared to the original pantograph.

Keywords: High-speed train; Pantograph; Bionic optimization; Aerodynamic drag; Performance analysis

http://dx.doi.org/10.6180/jase.202406_27(6).0009

1. Introduction

With the rapid development of high-speed railway, increasing attention has been devoted to the issues concerning comfort, safety and speed. The aerodynamic problems caused by increasing train speeds exert a significant impact on train components [1]. As the primary component of high-speed trains, the pantograph system with a complex shape is directly affected by the airflow on the roof during train operation. So the aerodynamic problems posed by the pantograph are particularly salient. According to relevant research, when the speed of a train exceeds 200 km/h, aerodynamic drag can account for over 70% of total drag [2]. When the train operates at high speeds, the pantograph's aerodynamic drag accounts for 8% to14% of the total aerodynamic drag of the train, which affects the quality of pantograph-catenary current collection [3]. In recent years, scholars have conducted a series of studies on the aerodynamic drag, noise and turbulence intensity of high-speed train pantographs. Yuan et al. [4] investigated a pantograph structure that incorporates symmetric elliptical structures on the carbon slide plate and pantograph rod, respectively, resulting in superior drag and noise reduction performance. Hu et al.[5] investigated the internal mechanism of drag reduction on shark groove surfaces through numerical simulation studies. It has been found that a pair of reverse "secondary vortices" exist on both sides of the groove's vertex, which can significantly attenuate turbulence intensity and achieve drag reduction. Liu et al. [6] utilized the k-ϵ turbulence model and broadband noise model to investigate the aerodynamics of the pantograph rod structure through computational simulations. They

discovered that the structure of the annularly corrugated groove member represents optimal bionic design, which significantly reduces both aerodynamic drag and noise. Wang et al. [7] used large eddy simulation to calculate the distribution characteristics and magnitude of aerodynamic noise in the flow field of a pantograph model. Based on the bionic structure of the flange, they optimized the current pantograph structure. The results showed that optimized pantograph demonstrated excellent aerodynamic performance, resulting in a reduction of pantograph tail vortex shedding and aerodynamic noise. Li et al. [8] established a high-speed pantograph aerodynamic model to investigate the operational characteristics of high-speed trains in knuckle-downstream and knuckle-upstream direction, providing a reference basis for pantograph design and optimization. Yan et al. [9] utilized computational fluid dynamics simulation technology to analyze the distribution of aerodynamic drag on the pantograph. By adding shells to both the slide plate and base, they proposed an optimization scheme that effectively reduces aerodynamic drag. Yang et al. [10] used Fluent software to calculate the aerodynamic drag of a pantograph at different speeds. They deduced the pantograph head is the main source of aerodynamic drag for the pantograph, and optimizing its structure can effectively reduce the aerodynamic drag.

Currently, there are many studies on reducing drag for high-speed train pantographs; however, few have explored the application of bionics technology in this area. Therefore, the shark skin was selected as the bionic object in this paper to design two types of bionic grooves that were integrated onto the lower surface of the slide plate. The numerical simulation method was used to investigate the influence of the slide plate structure on aerodynamic drag, pressure distribution and flow field characteristics of pantograph. In addition, the average rate of drag reduction for the two models was obtained, which is expected to serve as a reference for designing drag reduction in high-speed trains.

2. Bionic design of pantograph head

Bionic optimization refers to studying and imitating biological systems found in nature, drawing inspiration from them, constantly innovating in the process, and ultimately achieving or surpassing the functions of biological prototypes to solve various technical problems faced by humans. According to the principle of bionic design, it can be divided into morphological bionic, functional bionic, structural bionic, interface bionic and other forms [11].

2.1. Select the bionic object

Aquatic animals evolved to survive, eventually developing shapes and body surfaces that reduce drag [12]. Further research indicates that these large marine organisms possess a surface adorned with small-scale grooves, which effectively reduce hydrodynamic drag during rapid swimming and enable the organism to attain extremely high velocities [13]. Researchers have discovered that there are regularly arranged dermal denticles structures on the surface of shark skin by studying it, as shown in Fig. 1.

Fig. 1. The structure on the surface of shark skin.

It can be seen from Fig. 1 that the shield scales on the surface of shark skin are composed of small protrusions on the smooth surface and longitudinal micro-grooves in the flow direction. The design of ribs for drag reduction was inspired by the toothed structure on the surface of shark scales, which are also known as dermal denticles. The structure can reduce drag by lifting the fluid vortices in proximity to the bodies' surface [14]. Furthermore, based on the drag reduction mechanism of the "Second Vortex Group" theory and the "Protrusion Height" theory [15–17], it can be known that the non-smooth groove structure impedes instantaneous transverse flow caused by turbulent motion, reduces the turbulent flow in the boundary layer and enhances fluid vortex near the body surface. This ultimately decreases frictional drag between turbulence and wall surfaces.

2.2. Two-dimensional groove design

Two-dimensional groove geometric models, including arc-shaped grooves and V-shaped grooves, were established based on the micro-structure of shark surface and the drag reduction mechanism of the groove surface, as shown in Fig. 2 (a)-(b).

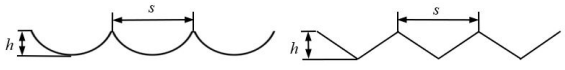

(a) Arc-shaped grooves **(b)** V-shaped grooves

Fig. 2. Two-dimensional groove geometric models.

In Fig. 2, h and s represent groove height and groove spacing respectively. When the groove spacing is within the range of 0 to 10 mm, irregular grooves can increase

drag. However, when it exceeds 10 mm, irregular grooves can reduce drag. The larger the gap, the more effective the reduction of drag. After comprehensive consideration, h is set to 5 mm and s is set to 20 mm in Fig. 2.

3. Numerical simulation

3.1. Geometric model

The pantograph used in this study is based on a genuine model of a standard electric multiple unit (EMU), which has a singular arm structure and dual carbon slide plates. The pantograph mainly consists of a pantograph head, upper and lower arms, a hinged system, a chassis, an insulator and a pantograph raising device. The dimensions of the pantograph model is 1.95 mx2 mx1.5m.

In this study, the front slide of the pantograph was selected for optimization to investigate the influence of carbon slides with different structures on its aerodynamic characteristics. Due to the two-dimensional grooves, wall friction can be effectively reduced. By coupling the groove structure to the lower surface of the pantograph slide plate, not only can drag on the pantograph head be reduced, but also its tail vortex area can be effectively controlled. The geometrical models of pantograph are shown in Fig. 3 (a)-(b).

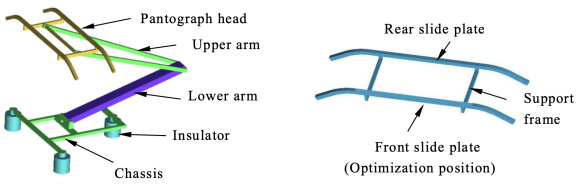

(a) Pantograph model **(b)** Pantograph head

Fig. 3. The geometrical model of pantograph.

The pantograph head has a total length of 1950 mm, with a working length of 1450 mm and a carbon slide plate length of 1430 mm. To ensure the current-receiving quality, it is necessary for the upper surface of the carbon slide plate to maintain contact with the contact line during pantograph operation [18]. Therefore, the lower surface of the carbon slide plate was optimized, while other parts of the pantograph were reasonably simplified and as much detail as possible was retained in the pantograph head. The half size of the pantograph head is shown in Fig. 4.

In Fig. 4, the half length of the pantograph head is 975 mm, its height is 368 mm, and the length of the skateboard is 515 mm. To save computing resources, the lower surface of carbon slide plate with a length of 880 mm was

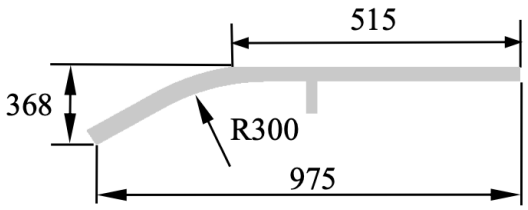

Fig. 4. The half size of the pantograph head (unit:mm).

optimized. Based on the original pantograph model, arc-shaped and V-shaped grooves were added to the lower surface of the carbon slide plate, resulting in two bionic pantograph models. Model A refers to the original pantograph geometrical model, Model B refers to the pantograph model with arc-shaped grooves on its lower surface of the carbon slide plate and Model C refers to the pantograph model with V-shaped grooves on its lower surface of the carbon slide plate. The bionic models of the three pantograph heads are shown in Fig. 5 (a)-(c).

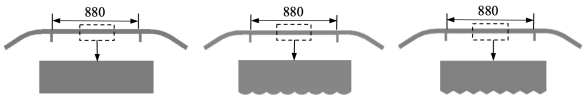

(a) Model A **(b)** Model B **(c)** Model C

Fig. 5. Three types of bionic pantograph head models (unit:mm).

3.2. Mathematical model

In this study, the pantograph's maximum speed is 350km/h and its windward Mach number is approximately 0.286 (less than 0.3). Therefore, an incompressible viscous flow field can be utilized. The continuity equation and momentum equation can be expressed as follows:

$$\frac{\partial u_j}{\partial x_j} = 0 \tag{1}$$

$$\rho\frac{\partial u_i}{\partial t} + \rho\frac{\partial\left(u_i u_j\right)}{\partial x_j} = -\frac{\partial p}{\partial x_i} + \frac{\partial \tau_{ij}}{\partial x_j} \tag{2}$$

Where u_i, u_j represent the air velocity components of the flow field surrounding the train; x_i, x_j represent the coordinate components, $i, j = 1, 2, 3$; ρ represents fluid density; t represents time; p represents the pressure; and τ_{ij} represents viscosity stress tensor.

Compared to DES and LES, the RANS method requires fewer computational resources while significantly enhancing computing speed. The continuity equation, momentum

equation, and energy equation are respectively expressed as follows:

$$\frac{\partial \rho}{\partial t}+\frac{\partial\left(\rho u_j\right)}{\partial x_j}=0 \tag{3}$$

$$\frac{\partial\left(\rho u_i\right)}{\partial t}+\frac{\partial\left(\rho u_i u_j\right)}{\partial x_j}=-\frac{\partial p}{\partial x_i}+\frac{\partial \tau_{ij}}{\partial x_j}+\frac{\partial}{\partial x_j}\left(-\rho \overline{u_i' u_j'}\right) \tag{4}$$

$$\begin{aligned}\frac{\partial(\rho e)}{\partial t}+\frac{\partial\left(\rho h u_j\right)}{\partial x_j}&=\operatorname{div}(k \operatorname{grad} T)\\&+\frac{\partial\left(u_i \tau_{ij}\right)}{\partial x_j}+\frac{\partial}{\partial x_j}\left(-\rho \overline{h' u_j'}\right)\end{aligned} \tag{5}$$

where e represents internal energy; k represents the thermal conductivity coefficient of the fluid; T represents temperature; and h represents enthalpy. In the $k-\varepsilon$ model, k and ε are two basic unknowns, where k represents turbulent kinetic energy and ε represents turbulent dissipation rate. The corresponding control equation can be defined as follows:

$$\frac{\partial}{\partial t}(\rho k)+\frac{\partial}{\partial x_i}\left(\rho k u_i\right)=\frac{\partial}{\partial x_j}\left[\left(\mu+\frac{\mu_t}{\sigma_k}\right)\frac{\partial k}{\partial x_j}\right]+P_k-\rho\varepsilon \tag{6}$$

$$\begin{aligned}\frac{\partial}{\partial t}(\rho \varepsilon)+\frac{\partial}{\partial x_i}\left(\rho \varepsilon u_i\right)&=\frac{\partial}{\partial x_j}\left[\left(\mu+\frac{\mu_t}{\sigma_k}\right)\frac{\partial \varepsilon}{\partial x_j}\right]\\&+C_{1\varepsilon}\varepsilon P_k/k-C_{2\varepsilon}\rho\varepsilon^2 P/k\end{aligned} \tag{7}$$

where P_k represents the turbulent kinetic energy generated by the mean velocity gradient $\left(P_k=\mu_t S^2\right)$; S represents the modulus of the strain rate tensor; C_μ, $C_{1\varepsilon}, C_{2\varepsilon}, \sigma_k, \sigma_\varepsilon$ all are empirical constants. Generally, $C_\mu = 0.09, C_{1\varepsilon} = 1.44, C_{2\varepsilon} = 1.92, \sigma_k = 1, \sigma_\varepsilon = 1.3$.

In this study, the Navier-Stokes equation for steady, viscous and incompressible flow and $k-\varepsilon$ turbulence model were employed to numerically solve the entire flow field around the pantograph [19]. The numerical simulations utilized a segregated, incompressible, unstructured finite-volume solver based on the STAR-CCM+. The SIMPLEC algorithm was used to couple the pressure and velocity fields. The convective term is discretized using the QUICK scheme with high-order accuracy, and the diffusion term is discretized using a central difference scheme with second-order accuracy [20].

3.3. The computational domain and its boundary conditions

The boundary conditions were established as follows. The left side of the computational domain was specified as the velocity inlet boundary condition. The right side of its was designated as the pressure outlet with an initial pressure of zero. Both sides of the computational domain were set as wall boundary conditions, and the top of its was defined as a symmetry boundary condition. The pantograph surface and ground were designated as non-slip boundary conditions. The computational domain is illustrated in Fig. 6 (a)-(b).

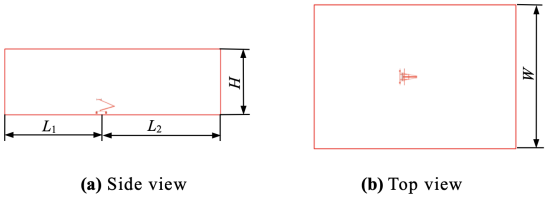

(a) Side view **(b)** Top view

Fig. 6. The computational domain.

In Fig. 6, W represents the width of the computational domain, which is 16 m, and H represents its height, which is 6 m. The distance between the velocity inlet and the pantograph center is $L_1 = 10$ m, and that between the pressure outlet and the pantograph center is $L_2 = 12$ m. The vertical clearance between the bottom of the pantograph and the ground is 0.2 m.

3.4. Computational grids

To ensure the accuracy of the calculation, three refinement regions were implemented in the flow field surrounding the pantograph. The smallest grids were located closest to the pantograph, and the surface grids of the pantograph were refined. Additionally, 10 prismatic layers were arranged on the pantograph surfaces with a thickness of approximately 0.2 mm for the first boundary layer close to the pantograph surfaces. Fig. 7 shows the configuration of the computational grids.

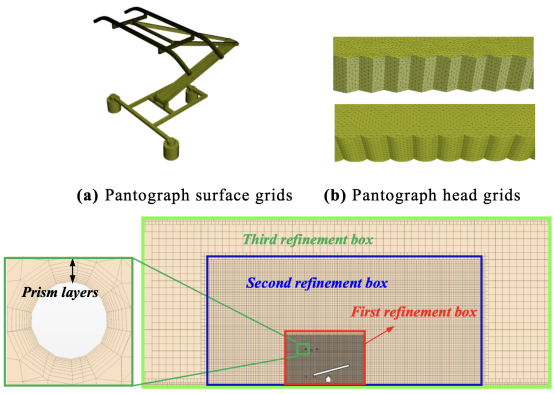

(a) Pantograph surface grids **(b)** Pantograph head grids

Fig. 7. Configuration of the computational grids.

3.5. Validation of calculation method

To examine the influence of mesh resolution on results, three distinct computational meshes (A, B and C) were used to compute the aerodynamic drag of the pantograph. Mesh A consists of 6.5 million cells, while Mesh B and Mesh C consist of 7.0 and 7.5 million cells, respectively. The numerical simulation results are shown in Table 1.

Table 1. Numerical simulation results.

Mesh type	Mesh number (million)	Aerodynamic drag (N)
A	6.5	2410.6
B	7.0	2385.6
C	7.5	2354.5

As presented in Table 1, the data error between Mesh B and Mesh A is 1%, while that between Mesh C and Mesh B is 1.3%. It can be inferred that as the number of grids increases, the variation in pantograph aerodynamic drag always remains within 2%. Therefore, it is appropriate to set the total number of grids within the calculation domain at 6.5 million.

To validate the accuracy of the numerical method adopted in this paper, a comparison was made between the data obtained from numerical simulation and wind experimental tunnel data [21]. The CX-PG pantograph model utilized in the wind tunnel experiment was also employed for numerical simulation. Drag calculations were performed using the aforementioned grid size and numerical methods. The mesh used for algorithm validation and the error between experimental and calculated results are shown in Fig. 8 (a)-(b).

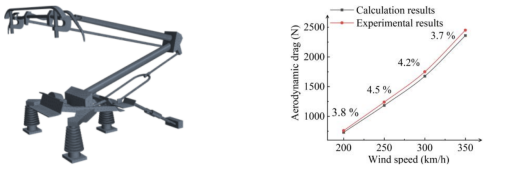

(a) Pantograph surface grids **(b)** The validation result

Fig. 8. Validation of the method.

As presented in Fig. 8 (b), the aerodynamic drag of the pantograph, calculated using the simulation method presented in this paper, is in good agreement with the experimental results, with errors always within 10%. This indicates that the numerical simulation method utilized in this paper can provide accurate calculation results.

4. Results and analysis

Due to the intricate structure of the pantograph, airflow passing through it will be seriously disturbed, so it is necessary to analyze the flow field around the pantograph. In order to study the influence of the bionic pantograph head on the flow field and aerodynamic load, the aerodynamic performance of pantograph can be analysed from two aspects: flow field and aerodynamic drag.

4.1. Analysis of the flow field

The flow field velocity diagrams for three kinds of pantographs at a flow velocity of 300 km/h are shown in Fig. 9 (a)-(c).

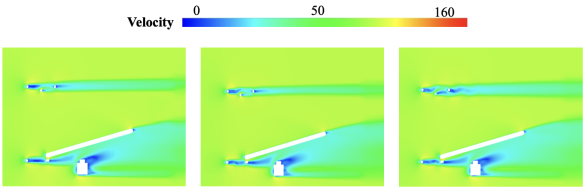

(a) Model A **(b)** Model B **(c)** Model C

Fig. 9. Flow field velocity diagram.

As shown in Fig. 9 (a), when the bottom of the pantograph carbon slide plate is smooth, boundary layer separation tends to occur at both upper and lower vertices of the pantograph head, causing airflow vortexes to form in the backflow zone. This often results in a higher velocity for the front pantograph head compared to the rear one, leading to an increase in aerodynamic drag. As shown in Fig. 9 (b) and (c), equipping the pantograph carbon slide plate with arc-grooves and V-grooves at its bottom can interfere with airflow, hindering the development of wake vortex and resulting in a smaller vortex area. Additionally, the separation point of the boundary layer is significantly shifted backwards. It can be inferred that the pantograph head with arc-shaped or V-shaped grooves under the carbon slide has better aerodynamic performance.

4.2. The aerodynamic drag

The aerodynamic drag of the pantograph head and the pantograph at various speeds was calculated through numerical simulation. To compare the aerodynamic drag characteristics of the three models, their respective aerodynamic drag was calculated at flow velocities ranging from 200 to 350km/h. The velocity-aerodynamic drag histograms of the three models are shown in Fig. 10 (a)-(b).

As can be seen from Fig. 10, the drag reduction effect of both arc-shaped grooves and V-grooves pantographs is es-

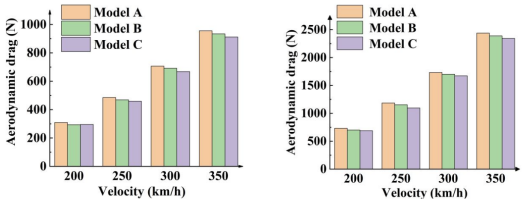

(a) Aerodynamic drag of pantograph head **(b)** Aerodynamic drag of pantograph

Fig. 10. Velocity-aerodynamic drag histograms.

sentially equivalent when running at a speed of 200 km/h. However, as the speed increases, the pantograph with V-shaped grooves exhibits better aerodynamic drag reduction effects than that with arc-shaped grooves. For the aerodynamic drag of the whole pantograph at running speeds of 250, 300, 350 km/h, the pantograph with V-shaped grooves demonstrates superior aerodynamic drag reduction effects compared to that with arc-shaped grooves. Both optimized models exhibit the best drag reduction effect at a speed of 350km/h.

To compare the drag reduction effects of two optimized pantograph models quantitatively, the average rate of drag reduction is defined as:

$$\gamma = \frac{D_1 - D_2}{D_1} \times 100\% \tag{8}$$

In formula 8, γ represents the average reduction rate of aerodynamic drag, D_1 represents the aerodynamic drag of the original pantograph model, D_2 represents the aerodynamic drag of the optimized pantograph model. The average reduction rates of aerodynamic drag for the pantograph head and pantograph were calculated, and the calculation results are shown in Table 2.

Table 2. The average reduction rate of aerodynamic drag.

Type of model	γ_a	γ_b
B	3.2%	2.6%
C	4.9%	4.7%

In Table 2, γ_a represents the average reduction rate of aerodynamic drag for pantograph head and γ_b represents the average reduction rate of aerodynamic drag for pantograph. Compared to the original model, optimized models have a drag reduction effect. However, it's more effective for the average rate of drag reduction of the pantograph head and the pantograph to set V-shaped grooves under the carbon slide plate. When the train's speed falls between 200 and 350 km/h, setting V-shaped grooves beneath the carbon slide plate, the average rate of drag reduction of pantograph head is 4.9% and the average rate of drag reduction of pantograph is 4.7%.

5. Conclusions

In this paper, the theories of non-smooth surface drag reduction and shark body surface bionics are used to study the performance of pantographs with different pantograph head. The conclusions are as follows:

1. Compared to the original pantograph, two optimized models can reduce aerodynamic drag. When the train is running at a speed of 200 350km/h, the average rate of drag reduction of pantograph head with V-shaped grooves under a carbon slide plate increased by 4.9%, and that of the pantograph increased by 4.7% compared to the original pantograph. The average rate of drag reduction of pantograph head with arc-shaped grooves under a carbon slide plate increased by 3.2%, and that of the pantograph increased by 2.6% compared to the original pantograph.

2. The shape of the pantograph head has a significant effect on the separation point of the boundary layer, wake flow and tail vortex area. Compared to the pantograph head with arc-shaped grooves, the pantograph with V-shaped grooves results in a more significant backward movement of the boundary layer separation point around the pantograph head, increased stability of wake flow, and a more prominent reduction in tail vortex area.

3. This study only investigates the aerodynamic drag performance of a pantograph with bionic non-smooth grooves under the surface of a carbon slide plate, but doesn't consider its noise performance. Therefore, we suggest that the aerodynamic drag and noise performance of pantograph should be comprehensively considered in subsequent studies.

Acknowledgments

This study was funded by Special Funds for Guiding Local Scientific and Technological Development by the Central Government (22ZY1QA005), Natural Science Foundation of Gansu (Grant No. 21JR11RA063) and Higher Education Innovation Foundation of Gansu (Grant No. 2021B-104).

References

[1] H. Song, J. Wu, Y. Wu, J. Zhen, and Q. Zhen, (2010) *"Study on aerodynamic effect on current receiving characteristics of high-speed pantograph"* **Electric Railway** **23**(1): 28–32.

[2] Z. Wu, Z. Xie, P. Wang, W. Ding, et al., (2020) *"Aerodynamic drag performance analysis of different types of high-speed train pantograph fairing"* **Journal of Applied Science and Engineering *23***(3): 509–519. DOI: 10.6180/jase.202009_23(3).0015.

[3] L. Zhang, J. Zhang, T. Li, and W. Zhang, (2017) *"Research on unsteady aerodynamic characteristics of pantographs in different positions of high-speed trains"* **Journal of Mechanical Engineering *53***(12): 147–155. DOI: 10.3901/JME.2017.12.147.

[4] X. Yuan, X. Miao, T. Yuan, and J. Yang, (2021) *"Aerodynamic noise analysis of high-speed train pantograph and study on noise reduction of pantograph head"* **Journal of the China Railway Society *43***(12): 38–48.

[5] H. Hu, G. Pan, B. Song, and Z. Mao, (2004) *"Numerical analysis of near-wall fluid field on grooved surface under water"* **Chinese quarterly of mechanics *25***(1): 96–100.

[6] H. Liu and Z. Xu, (2018) *"Study on drag and noise reduction of pantograph rods based on bionic non-smooth structures"* **Noise and Vibration Control *38***(S1): 269–272.

[7] Y. Wang, J. Zhou, D. Gong, and H. Liu, (2018) *"Study on bionic noise reduction and aerodynamic noise distribution characteristics for high-speed train's pantographs"* **Noise and Vibration Control *38***(Z1): 348–352.

[8] T. Li, D. Qin, D. Zou, J. Zhang, and W. Zhang, (2020) *"Study on aerodynamic characteristics and comparisons of high-speed pantograph in knuckle-downstream or knuckle-upstream direction"* **Journal of Mechanical Engineering *56***(4): 177–184. DOI: 10.3901/JME.2020.04.177.

[9] Y. Yan, X. Xu, X. Wang, H. Geng, and S. Huang, (2022) *"Simulation optimization study on aerodynamic drag reduction of high speed pantograph"* **Mechanics in Engineering *44***(2): 276–284.

[10] K. Yang, F. Ma, X. Zhu, and J. Li, (2015) *"Analysis of aerodynamic characteristics of pantograph based on Fluent"* **Electric Railway** (4): 14–16.

[11] L. Zhou, D. Dai, and X. Chen, (2014) *"The Application of Bionics Design in The Design of Chinese High Speed Train"* **School of Architecture and Art, Central China University** (9): 57–58.

[12] J. Du, M. Gong, A. Tian, N. Gao, and Z. Li, (2014) *"Study on the drag reduction of the high-speed train based on the bionic non-smooth riblets"* **Journal of Railway Science and Engineering *11***(5): 70–76. DOI: 10.19713/j.cnki.43-1423/u.2014.05.013.

[13] Z. Wang, (2015) *"Numerical simulation of high-speed train drag reduction mechanism based on bionics"* **Urban Mass Transit** (1): 28–31. DOI: 10.16037/j.1007-869x.2015.01.007.

[14] L. Qin, C. Gong, H. Sun, H. Xi, F. J. Mawignon, F. Guo, and G. Dong, (2022) *"Review of research on drag reduction of non-smooth surface"* **Surface technology *51***(8): 107–122. DOI: 10.16490/j.cnki.issn.1001-3660.2022.08.009.

[15] B. E and S. C, (1985) *"A combined visualization-anemometry study of the turbulent drag reducing mechanisms of triangular micro-groove surface modifications"* **AIAA Journal *87***(6): 85–548.

[16] D. Bechert and M. Bartenwerfer, (1989) *"The viscous flow on surfaces with longitudinal ribs"* **Journal of fluid mechanics *206***(1): 105–129.

[17] A. Lang, P. Motta, M. L. Habegger, R. Hueter, and F. Afroz, (2011) *"Shark Skin Separation Control Mechanisms"* **Marine Technology Society Journal *45***(4): 208–215. DOI: 10.4031/MTSJ.45.4.12.

[18] R. Li, N. Zhou, W. Zhang, G. Mei, and Z. Chen, (2012) *"Calculation and analysis of pantograph aerodynamic uplift force"* **Journal of the China Railway Society *34***(8): 26–32. DOI: 10.3969/j.issn.1001-8360.2012.08.005.

[19] H. Tian. *Train Aerodynamics*. Beijing: China Railway Publishing House, 2007.

[20] J. Wang, G. Minelli, T. Dong, K. He, and S. Krajnovi, (2020) *"Impact of the bogies and cavities on the aerodynamic behaviour of a high-speed train. An IDDES study"* **Journal of Wind Engineering and Industrial Aerodynamics *207***: DOI: 10.1016/j.jweia.2020.104406.

[21] S. Fu, D. Chen, J. Liang, and Y. Ma, (2013) *"Investigation on wind tunnel tests of aerodynamic characteristics of high-speed pantograph"* **Railway Locomotive & Car *33***(3): 123–126.